Modes and break periods of electrowetting liquid bridge

Mohsen Torabi, Ahmed A. Hemeda, James W. Palko, Yu Feng, Yong Cao, and Yanbao Ma

Phys. Rev. E **100**, 033102 — Published 11 September 2019

DOI: 10.1103/PhysRevE.100.033102

Modes and break periods of electro-wetting liquid bridge

Mohsen Torabi[1†], Ahmed A. Hemeda[1,2†], James W. Palko[1], Yu Feng[3], Yong Cao[3] and Yanbao Ma[1*]

[1]School of Engineering, University of California, Merced, CA 95343, USA

[2]Aerospace Engineering Department, Cairo University, 12613 Egypt

[3]Harbin Institute of Technology, Shenzhen, Guangdong 518055, People's Republic of China

Abstract

In this paper, we propose a microscale liquid oscillator using electrowetting-on-dielectric (EWOD). Specifically, a mesoscale liquid bridge (LB) between two horizontal surfaces with EWOD is considered. When EWOD is applied, the solid surface becomes more hydrophilic, and hence the contact angle (CA) is reduced. Following the activation of EWOD, the LB can remain connected or it can break into either symmetric or asymmetric shapes depending on the initial liquid volume and wettability of the two surfaces. The LB dynamics activated by EWOD is studied using the multi-body dissipative particle dynamics (MDPD) method. Our numerical results show that the behavior of an LB under EWOD can be interpreted via three modes. In the first mode, the LB does not break after applying EWOD. In the second mode, the LB breaks and does not re-form. The third mode happens when, depending on the interplay of the volume of the liquid and CA manipulation, the LB continuously breaks, recoils, and re-forms. For asymmetric cases, it was observed that the LB may completely detach from one surface and may not re-form the LB again. It was also observed that decreasing the wettability of a surface, for cases with a continuous breaking/reformation behavior, increases the connecting time interval and decreases the breaking time interval in one break/re-form cycle. The results provided in this investigation facilitate fundamental understanding of LB dynamics and their application for the design of microscale liquid oscillators using EWOD.

Keywords: Electrowetting-on-dielectric; Liquid bridge; Switchable wettability; Digital microfluidic; Mesoscale.

† These authors contributed equally to this work

*Address correspondence to Yanbao Ma, email: yma5@ucmerced.edu; Tel.: 209-228-4046

1. Introduction

Microfluidics combines both the science and the technology of manipulating and controlling fluids in small scales, usually in the range of microliters to picoliters [1]. Digital microfluidics is an attractive branch of microfluidics, providing a platform for lab-on-a-chip systems [2][3]. By using various techniques to modify different characteristics of fluids and surfaces such as wettability, droplets are successfully moved, mixed, separated or stored on a platform with a set of microscale devices [2][3][4]. The tendency for wetting of a surface can be modified by various approaches such as introducing roughness [5] or changing chemical properties of the surface [6][7][8]. The surface morphology and chemical properties provide certain boundary conditions which guide the liquid to the most energetically minimized position, and hence shape the desired configuration [9][10]. A downside of chemical and topographical patterns is their fixed nature, which means that these patterns cannot be modified after construction [11].

The wettability of a surface can also be modified by artificially increasing the energy of a surface using an electrostatic force between the surface and liquid [12][13]. Unlike chemical and topographical patterns, electrostatic forces provide a great degree of switchability and long term durability [14][15]. This technique, commonly called electro-wetting (EW), was introduced by Lippmann in 1875 [11]. To limit current and bypass electrolysis in the liquid at high actuation voltages, the conductive liquid and the metallic electrode should be separated. This has been addressed via electrowetting-on-dielectric (EWOD) by Berge [16]. By using EWOD, the droplet is controlled by the applied voltage at the electrode just below the substrate surface. By applying the voltage, a charge at the liquid-solid interface is created and the surface tension is locally reduced. This generates a flow in the direction of low surface tension, and consequently, the contact angle (CA) of the liquid is modified to a reduced value. To fully utilize the potential of EWOD and to deal with more complex situations, various improvements and developments such as optoelectrowetting have been sought [17].

Given EWOD's precise controllability, accurate modification of values of CA for a liquid droplet on a surface can be accomplished. It has been shown that by applying different voltages, different CAs, reduced to less than 20^{o} can be achieved [18][19]. Although EWOD is still a new technique, there have been extensive investigations on this topic due to its potential for both scientific and industrial applications. By way of fundamental investigations, firstly, various experiments on the relation between CAs and applied voltages have been carried out [18][19]. EW-induced droplet spreading

and detachment in conventional ambient [20][21][22] and oil environments [23] for stationary configurations have been investigated. The effect of voltage magnitude on the advancing and receding CAs was also studied [24]. Controlling the CA of liquid drops on different surfaces via EWOD was proven to be effective to control the permeability of porous structures [25] and to assist bubble detachment from a liquid film [26]. It was also shown that by controlling the applied voltage between two surfaces of a wedge, the position and shape of liquid drops confined in the wedge can be precisely controlled [27]. An interesting recent experiment also showed that by choosing specific parameters in a precisely designed configuration, the angle of ballistic ejection of liquid drops can be accurately manipulated via electrostatic forces [28].

EWOD has also found numerous practical applications from smart optics [29] to energy harvesting [30] and liquid resonators [31]. Shortly after the introduction of EWOD in 1993 [16], it was employed in cameras to change the focal length of lenses [32]. By taking advantage of manipulating the air-water interface via EW, a centimeter-sized boat without complicated propulsion mechanisms was invented [33]. Because of the precisely controllable nature of EW, reconfigurable optofluidic slits without mechanically moving parts have also been realized [34]. EW has shown extensive applicability in three-dimensional digital microfluidics such as accurate manipulation and mixing of different droplets with various chemical properties [35]. While the above-mentioned applications have used EW in an actuation manner, a similar application showed the capability of this phenomenon for harvesting energy in small scale geometries [30][36].

As mentioned before, by applying EWOD via a voltage difference between the upper and lower surfaces, the solid surfaces become more lyophilic via an electrostatic force applied on the liquid-solid interfaces. This dynamic force consequently reduces the CA of the droplet and causes the droplet to deform. By removing the applied voltage on the system, the liquid would recoil and tend to recover its original configuration. If the potential energy within the liquid droplet corresponding to the surface tension is sufficient, the droplet may detach from the surface [22][28]. On the other hand, if the process is happening in a confined environment the droplet may jump from one surface to another, which has been recently demonstrated [35]. Another potential configuration is a capillary bridge between two surfaces [27][11][37]. If a liquid bridge (LB) forms between two horizontal EW surfaces, the meniscus of the bridge can be modified by applying a voltage between the upper and lower walls, and the LB may break [38]. After bridge breaking, the applied voltage appears mainly across the gap reducing the electric field at the liquid/solid interfaces, and the liquids on each surface

would recoil. Depending on the maximum recoiling/jumping height, the two liquid parts may touch each other, and the bridge formation and disruption may continue.

Although there has been an experimental investigation on the behavior of an LB under electrostatic forces [38], there is no comprehensive analysis of this phenomenon. An LB under electrostatic forces may change its shape and form a neck somewhere between the upper and lower surfaces. Depending on the original wettability of the upper and lower surfaces, the LB can be symmetric or asymmetric. Hence, by introducing EW, an LB may form a symmetric or asymmetric neck and may break.

The present investigation deals with a mesoscale LB-EWOD system to shed light upon the different break mechanisms and modes of the LB, and to provide fundamental understanding on different stages of this phenomenon. To model a mesoscale LB, the multi-body dissipative particle dynamics (MDPD) method is used. Simulation details and features of MDPD are elaborated in section **2**. Then, the investigated configuration and its geometrical specifications are given in section **3**. Section **4** provides an in-depth illustration and discussion on the various modes and styles of the breakup or re-configuration of the bridge. Finally, section **5** gives conclusions and remarks regarding the implications of these processes for the application of EWOD.

2. MDPD Simulation

2.*1. Governing Equations*

MDPD is an extension to the mesh-free, coarse-grained molecular dynamics (MD) dissipative particle dynamics (DPD) simulation approach [39]. Unlike DPD, MDPD is capable of simulating unconfined geometries. In this method, a cluster of several molecules forms each particle. This method also includes Brownian motions within the simulation, which are crucial at these small scales. The length and time scales in MDPD are between atomistic and continuum approaches [40][41], which is an advantage of this method. Ghoufi and Malfreyt [42] have shown that the computational cost of MDPD is 20 times lower than MD simulation to achieve the same real time.

To model the motion of each MDPD particle or "bead," Newton's second law is used as follow:

$$\frac{\mathrm{d}\vec{r}_i}{\mathrm{d}t} = \vec{\upsilon}_i \tag{1}$$

$$m_i \frac{\mathrm{d}\vec{\upsilon}_i}{\mathrm{d}t} = \vec{f}_i = \sum_{j \neq i} \left(\vec{f}_{ij}^{C} + \vec{f}_{ij}^{D} + \vec{f}_{ij}^{R} \right) + \vec{g} \tag{2}$$

where $\vec{r}_i$, $\vec{\upsilon}_i$ and $\vec{f}_i$ denote the ith bead's position, velocity, and total force, respectively. The external body force exerted on each particle is incorporated into the model by parameter $\vec{g}$, which can be neglected here because of the particle size and operating condition [43][40][44]. The conservative force $\vec{f}_{ij}^{C}$, dissipative force $\vec{f}_{ij}^{D}$ and random force $\vec{f}_{ij}^{R}$ are given by [41][45]:

$$\vec{f}_{ij}^{C} = A_{ij}\omega_c(r_{ij},R_c)\vec{e}_{ij} + B_{ij}(\bar{\rho}_i + \bar{\rho}_j)\omega_c(r_{ij},R_d) \quad (3)$$

$$\vec{f}_{ij}^{D} = -\gamma\omega_D(r_{ij},R_c)\left(\vec{e}_{ij}\cdot\vec{\upsilon}_{ij}\right)\vec{e}_{ij} \quad (4)$$

$$\vec{f}_{ij}^{R} = \varphi\omega_R(r_{ij},R_c)\theta_{ij}\Delta t^{-1/2}\vec{e}_{ij} \quad (5)$$

where the subscript j stands for neighbor particles to the particle i (i.e., $j \in S_i$, see for instance Fig. 1c). Also, $r_{ij} = \left|\vec{r}_{ij}\right|$, $\vec{r}_{ij} = \vec{r}_i - \vec{r}_j$, $\vec{e}_{ij} = \vec{r}_{ij}/\left|\vec{r}_{ij}\right|$ and $\vec{\upsilon}_{ij} = \vec{\upsilon}_i - \vec{\upsilon}_j$ .A_{ij} and B are the attractive and repulsion force amplitudes with weighting functions of ω_C with two different cut-off radii R_c and $R_d = 0.75R_c$, where $\omega_C\left(r_{ij},R_c\right) = \max\left(1 - r_{ij}/R_c, 0\right)$. γ and φ are the dissipative and random force amplitudes. Stability conditions require that $\omega_R = \sqrt{\omega_D}$ and $\varphi^2 = 2\gamma k_B T$ where k_B is Boltzmann constant and T is the temperature of the system. The parameter θ_{ij} is sampled from a Gaussian white noise distribution with unit bandwidth, and Δt is the time step. Warren proposed an empirical density-dependent conservative force formula with cut-off range R_d. The local density-function is given by [46]:

$$\bar{\rho}_i = \frac{15}{2\pi R_d^3}\sum_{j\neq i}\left(1 - r_{ij}/R_d\right)^2 \quad (6)$$

More explanations of forces and parametric values of MDPD can be found in, e.g.[47].

2.2. *Fluid-Structure Interaction*

In our MDPD implementation, the substrate particles are assumed to be frozen for simplicity [48][49], but their interaction with the fluid is considered. As shown above, forces between beads are soft and short-range interactions [50]. This allows large time steps for the interaction of particles within the system. However, unlike the hard potentials in MD, the soft interaction between beads would not prevent fluid beads from penetrating into walls [51]. To prevent penetration of the fluid beads into the solid part of the system and to ensure the no-slip boundary condition, the bounce-back treatment has been implemented in this work. A simple mathematical manipulation for bounce-back boundary condition for a flat horizontal wall can be written as follow:

$$\vec{\upsilon}_{i,m} = -\vec{\upsilon}_{i,p} \quad (7)$$

$$\vec{r}_{i,m} = 2\tau_m\left(\vec{r}_{i,o} - \vec{r}_{i,p}\right) + \vec{r}_{i,p} \quad (8)$$

where

$$\tau_m = (z_w - z_p)/(z_o - z_p) \tag{9}$$

In the above equations the subscripts m, 0, p and w denote modified, old, predicted and solid wall, respectively. Also, the parameter z is the vertical component of $\vec{r}_i$ which is used to calculate the parameter τ_m [51]. Note that the above-mentioned equations (Eqs. 8 and 9) are the parametric form of a straight line in 3D.

To change the interaction of the fluid with solid walls for different static or dynamic behaviours, only one interaction parameter is modified. This parameter is usually the attraction force amplitude in the conservative force, i.e. A_{ij}, between fluid and solid beads, A_{s1} [47]. Hence, the rest of the interaction parameters for the solid/fluid particles remain constant. The parametric values used in this investigation and their representative values in the physical domain have been tabulated in Table 1.

Table 1. Parametric values used in MDPD simulation.

Parameter	**Symbol**	**DPD values**	**Physical values for water/glycerol mixture** [52]
Particle mass	m	1.0	5.43×10^{-16} kg
System energy	k_BT	1.0	---
Cut-off radius of attractive force	R_c	1.0	---
Cut-off radius of repulsive force	R_d	0.75	---
Attraction parameter (liquid-liquid)	$A_{\ell\ell}$	-40	---
Repulsion parameters	$B_{\ell\ell}$, $B_{s\ell}$	25	---
Amplitude of random force	φ	6.0	---
Time step	Δt	0.01	2.49×10^{-9} s
Fluid bead density	ρ	6.10	$1{,}137\,\mathrm{kg\cdot m^{-3}}$
Liquid-vapor surface tension	σ	7.30	$0.064\,\mathrm{N\cdot m^{-1}}$
Liquid kinematic viscosity	υ	7.45/6.1	$10^{-5}\,\mathrm{m^2\cdot s^{-1}}$

2.*3. Dimensional Analysis*

The MDPD parameters used in the present investigation are provided in Table 1. Properties of the working fluid are expressed in the dimensionless form with the transformation to physical units given below. Assuming the fluid density, kinematic viscosity, and surface tension in SI unit are d^*, υ^* and σ^*, respectively, the conversion length L_{DPD}, mass M_{DPD}, and time T_{DPD} are obtained using the following formulae:

$$L_{DPD} = \frac{d^*}{d}\left(\frac{\upsilon^*}{\upsilon}\right)^2 \frac{\sigma}{\sigma^*} \tag{10}$$

$$T_{DPD} = L_{DPD}^2 \frac{\upsilon}{\upsilon^*} \tag{11}$$

$$M_{DPD} = \frac{d^*}{d} L_{DPD}^3 \tag{12}$$

In Table 1, the last three rows (d , σ and υ) are devoted to the values of fluid density, kinematic viscosity and surface tension in the DPD and physical units. For example, by considering a water/glycerol mixture with wt % of 59 as the working fluid [52], the DPD unit length can be then calculated as :

$$L_{DPD} = \frac{1139[\mathrm{kg\cdot m^{-3}}]}{6.1[\mathrm{DPD\,unit}]}\left(\frac{10^{-5}\,\mathrm{m^2\cdot s^{-1}}}{7.45/6.1[\mathrm{DPD\,unit}]}\right)^2 \frac{7.3[\mathrm{DPD\,unit}]}{0.064\,\mathrm{N\cdot m^{-1}}} \tag{13}$$

which results in a physical length of $L_{DPD} \approx 1.43$ μm for the unit length in non-dimensional "DPD units". By following the same notion, the unit time and mass are calculated as $T_{DPD} \approx 2.49\times10^{-7}$ s and $M_{DPD} = 5.43\times10^{-16}$ kg. These values are much larger than the unit values in MD simulations [53]. It should be mentioned that by decreasing the viscosity, density, and surface tension of the fluid in the above equations, the unit length of each DPD can be decreased to the order of nanometers.

3. Configuration and Solution Algorithm

An LB between two horizontal plates is considered in this investigation. In EWOD experiments, the inner surfaces of metallic plates are covered by a thin layer of dielectric materials, e.g., SU-8, to avoid electrolysis, followed by a hydrophobic layer, e.g., Polytetrafluoroethylene [54][55]. The upper and lower plates are then connected via an applied voltage. Depending on the wetting properties of the upper and lower surfaces, the initial configuration of the bridge can be either symmetric or asymmetric. The schematic of two LB-EWOD systems is shown in Fig. 1. By closing the electric circuit, the LB in Fig. 1a deforms symmetrically, and the LB in Fig. 1b deforms asymmetrically. For sufficient applied voltage, the LBs may break in a symmetric/asymmetric fashion corresponding to the form of the original bridge. Once the bridge breaks, the applied voltage is mainly manifest across the gap due to the very low dielectric constant of air or vapor filling the gap compared to the liquid. This results in a reduction in the effect of electric field on wettability at the liquid/solid interface. This investigation models similar configurations and phenomena by applying switchable wettability criteria on the upper and lower surfaces by changing A_{s1} in the MDPD simulation. Figure 1c shows

the solution algorithm for modelling the LB between two surfaces under investigation. The details of this algorithm will be given later in Sec. 4.2. The LB's height, i.e., the gap between the horizontal surfaces, is $H_{LB} = 15$ DPD length (or $H_{LB} = 21.5$ μm), and the three $W_s \times D_s \times T_s$

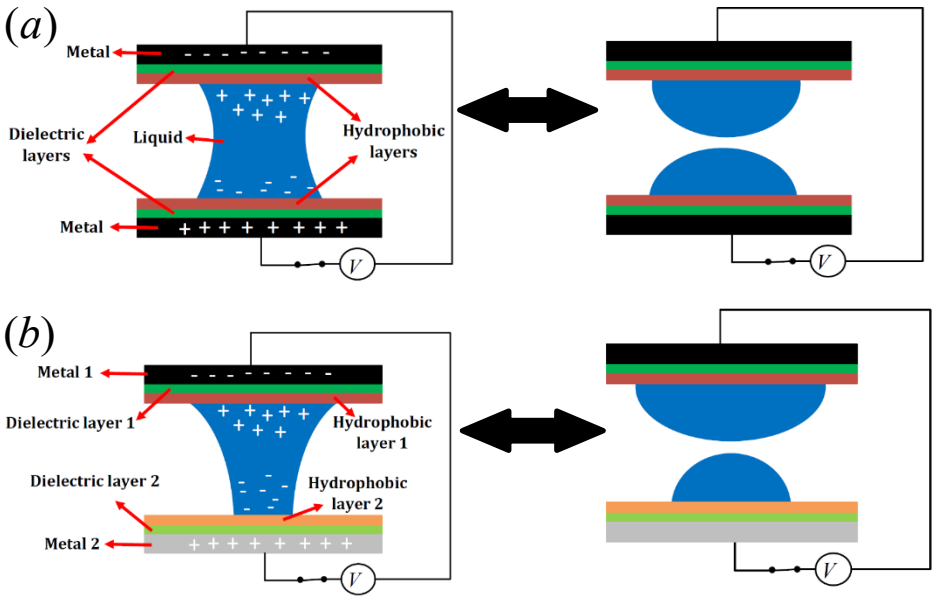

(c)

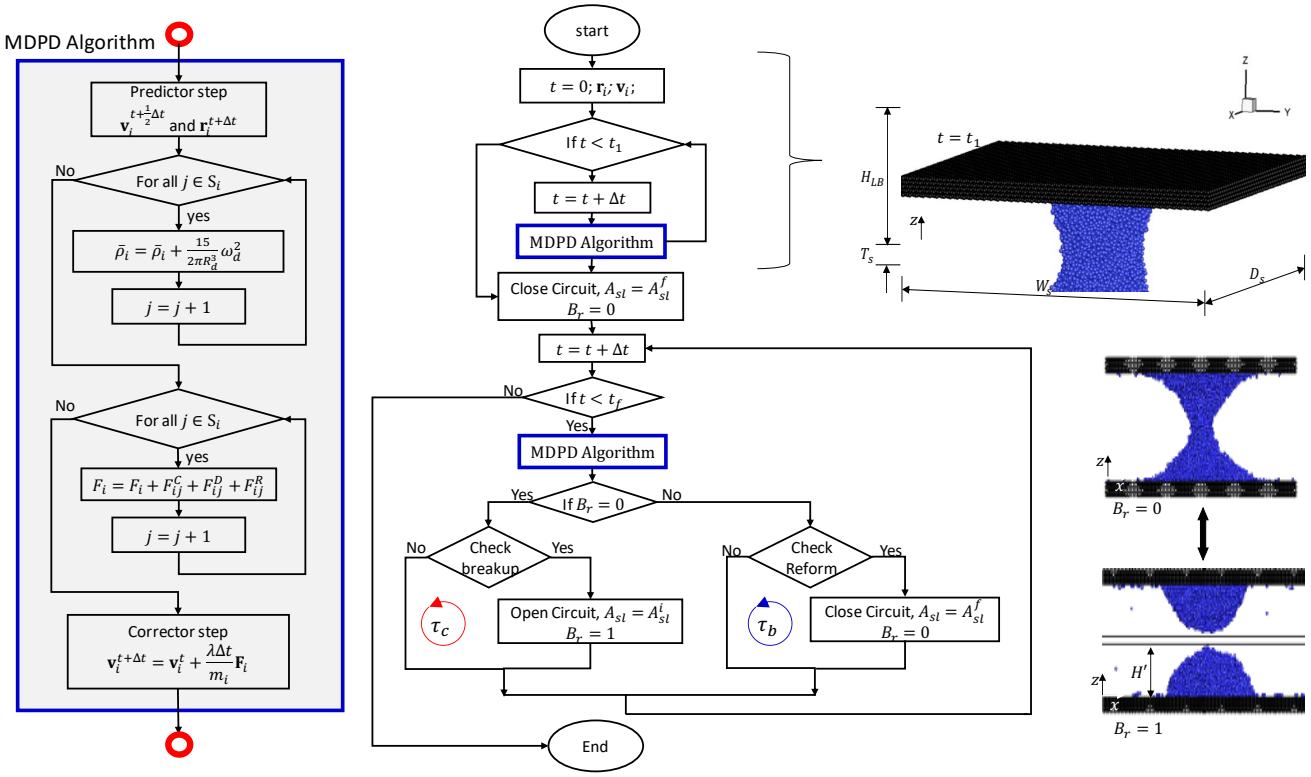

Fig. 1. Schematic of the liquid bridge and its disruption due to electro-wettability phenomenon. (a) Symmetric and (b) asymmetric induced electro-wetting. (c) The solution algorithm of MDPD, and the present LB-EWOD models. The LB-EWOD examples in (c) include the configuration and dimensional parameters of the present MDPD simulation, and two cases when $B_r = 0$ and $B_r = 1$.

dimensions of the upper and lower plates in MDPD simulations are kept constant at $40\times40\times3$, respectively, for all of the case studies. These dimensions are shown in Fig. 1c. Three different numbers of MDPD beads for the liquid phase, i.e., liquid volumes V, are considered for each scenario. The number of liquid and solid beads in each case are given in Table 2.

Table 2. Number of liquid and solid particles in each case.

Case Number	**Liquid beads/volume, V**	**Solid beads/volume, V**
Case 1	5,508/2,684 μm^3	42,320/20,625 μm^3
Case 2	9,792/4,772 μm^3	
Case 3	13,328/6,522 μm^3	

4. Results

4.*1. Validation*

For validation purpose, the effect of $A_{s\ell}$ on the CA of a static droplet on a horizontal flat wall is reported. Figure 2 provides a thorough illustration of this effect. The inset figures show liquid droplets on lyophilic or lyophobic surfaces. Figure 2 shows excellent agreement between the present results for the contact angle of a droplet and the reported MDPD study by Chang et al. [56]. As a reference for wettability characteristics of the surfaces considered in the following analyses, the corresponding CA for each $A_{s\ell}$ has been also provided in Table 3.

Table 3. CA versus $A_{s\ell}$ for a liquid droplet on a solid surface using the MDPD method.

$A_{s\ell}$	**CA**	$A_{s\ell}$	**CA**
-10	167±5.7	-30	81±2.2
-15	147±4.1	-35	55±1.5
-20	126±4.0	-40	26±1.0
-25	107±3.8		

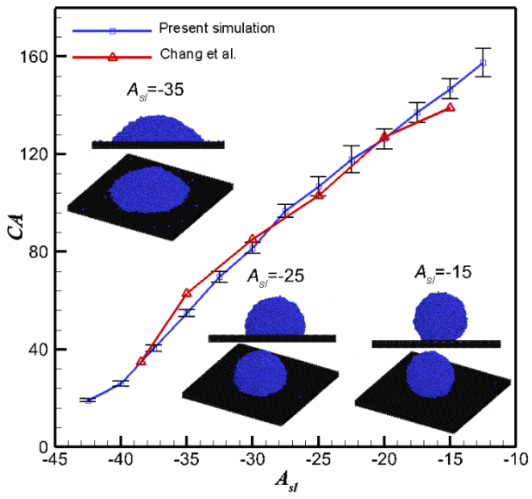

Fig. 2. Comparison of the contact angle of a droplet on a wall using the present MDPD method and provided data by Chang et al. [56].

4.2. *Symmetric LB*

In this section, a comprehensive analysis of symmetric LB-EWOD is provided. As mentioned before, three different volumes for the liquid phase are considered for each parametric study, which are given in Table 2. After assigning an initial $A_{s\ell}$ value on each surface, a final $A_{s\ell}$ value is assigned to each surface to modify the LB meniscus and possibly break the bridge. Hereafter, the superscript i and f for $A_{s\ell}$ represents the initial and final $A_{s\ell}$ values, respectively. Figure 3, which represents the analysis of the symmetric EWOD system in Fig. 1a, shows examples for different modes of LB and its response to a sudden change of $A_{s\ell}$ value on both surfaces. These modes result from the interplay of $A_{s\ell}^{i}$, $A_{s\ell}^{f}$ and LB volume as will be discussed later. From $t=0$ to $t=t_1=100$ DPD time units the values for wettability of the upper and lower surfaces are kept at A_{s1}^{i}. t_1 should be large enough to ensure convergence to a steady state. Then, the dynamic process begins at $t=t_1=100$ by switching the A_{s1}^{i} to A_{s1}^{f}. A new variable, B_r, is defined for the LB breakup or reformation. $B_r=0$ means that the LB is intact, whereas $B_r=1$ indicates breaking of the bridge. In order to determine B_r, we divide the space between the parallel plates into $N=15$ vertical bins ($H_{LB}=15$ DPD), then the average local density is calculated within each bin. If this average local density approaches zero in any of these bins, the LB is considered broken, i.e., $B_r=1$. This approach was adopted from local density

calculations in molecular dynamics [57][58]. If the LB breaks, the electric field is dramatically reduced at the liquid/solid interface, and A_{s1}^{f} changes back to A_{s1}^{i}, causing the liquid to recoil (see for instance Fig. 1c). The periods, τ_c (when $B_r = 0$) and τ_b (when $B_r = 1$), are calculated within each loop with the same value B_r. This will be discussed later.

Generally speaking, there are three modes for the behavior of a symmetric LB under the influence of EWOD. These three modes are shown in Figs. 3a-c based on the LB's center of mass (CM) while EW is applied. The corresponding CAs are reported in Fig. 4. If a low voltage is applied or if the initial CA is already very low, the modified contact angle causes a marginal change on the meniscus of the LB, and hence the LB will not break (Mode 1 in Fig. 3a). However, if the applied voltage is enough the CA significantly changes and finally the LB breaks. This happens in Figs. 3b (Mode 2) and 3c (Mode 3). In Fig. 3b the volume of the liquid and/or the initial CA on each surface hinders the LB reformation after the disruption. These two parameters of the system provide a favorable situation in Fig. 3c for LB reformation after the disruption. Therefore, in Fig. 3c the LB continues to break and re-form with a certain period. Supplementary Movie 1 shows the time history of the LB for Mode 3 (Fig. 3c). While the previous three modes have been analysed after getting a stable LB for $A_{s\ell}^{i}$ on each surface, it is also possible that by applying a specific $A_{s\ell}^{i}$ on the surfaces, the LB would not be stable between two surfaces. This is mainly because of the small volume of the liquid and mainly happens for Case 1, which has 5,508 liquid beads. The CM evolution of a sample case for this scenario are illustrated in Fig. 3d, but it is not considered as one of the LB modes since it is not a stable LB. Figure 4 serves as a companion to Fig. 3 and provides information regarding local dynamic CA of the LB with respect to the lower horizontal wall versus time. Note that the errorbar in Fig. 4 gives the standard deviation for the contact angle at 100 time steps around mean time, and this change is due to the random force. As can be seen from Fig. 4b and 4c, before LB breaking, the contact angle reaches its minimum value. The break dramatically reduces the electric field on the solid/liquid interface, i.e., $B_r = 1$ and $A_{s\ell}$ returns to $A_{s1} = A_{s1}^{i}$. Hence. the CA suddenly increases, and the upper and lower liquids recoil. If the separated liquid parts on upper and lower walls later connect to each other, which happen in Fig. 4c, the bridge forms again, CA decreases, and the cycle continues.

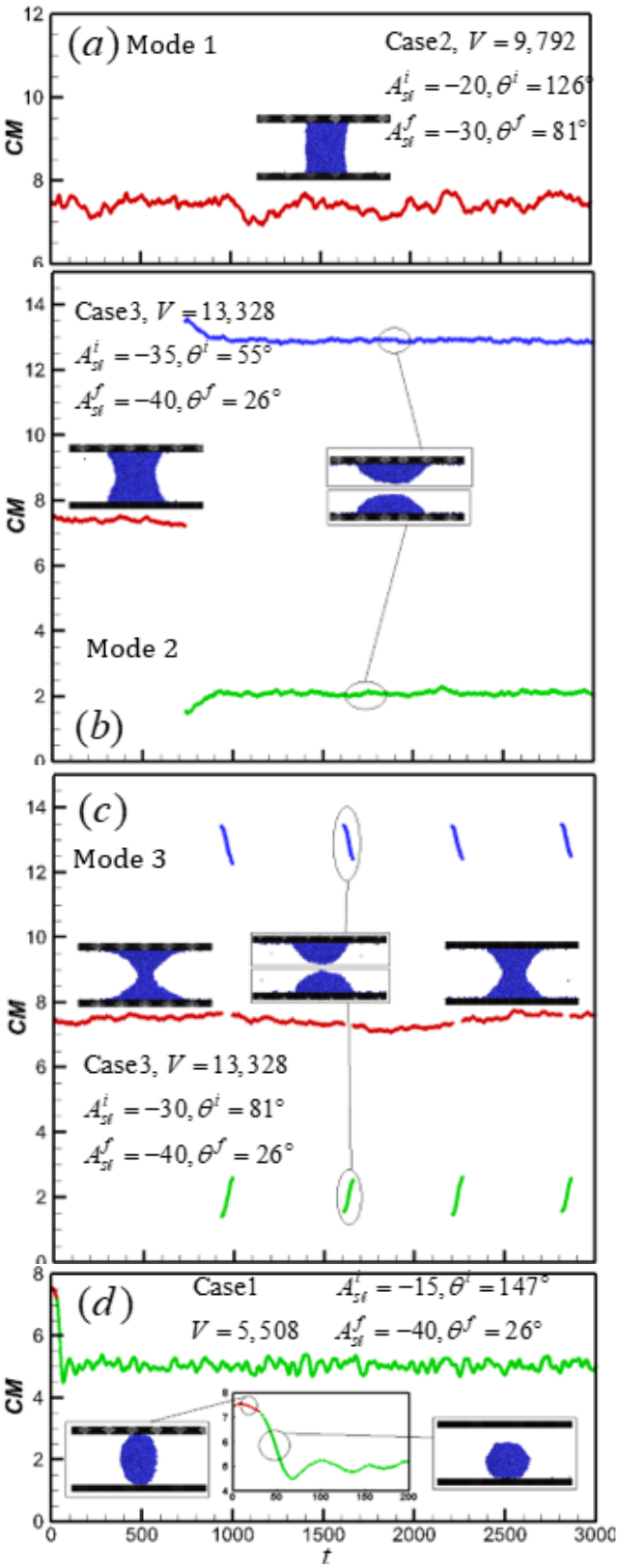

Fig. 3. Center of mass (CM) for different models of the electro-wetting bridge. (a-c) Modes 1 to 3, respectively. (d) Example unstable liquid bridge for high original CA. The CM position shown as red,

blue, and green curves are for the complete bridge and the upper and lower portions of the droplet, respectively.

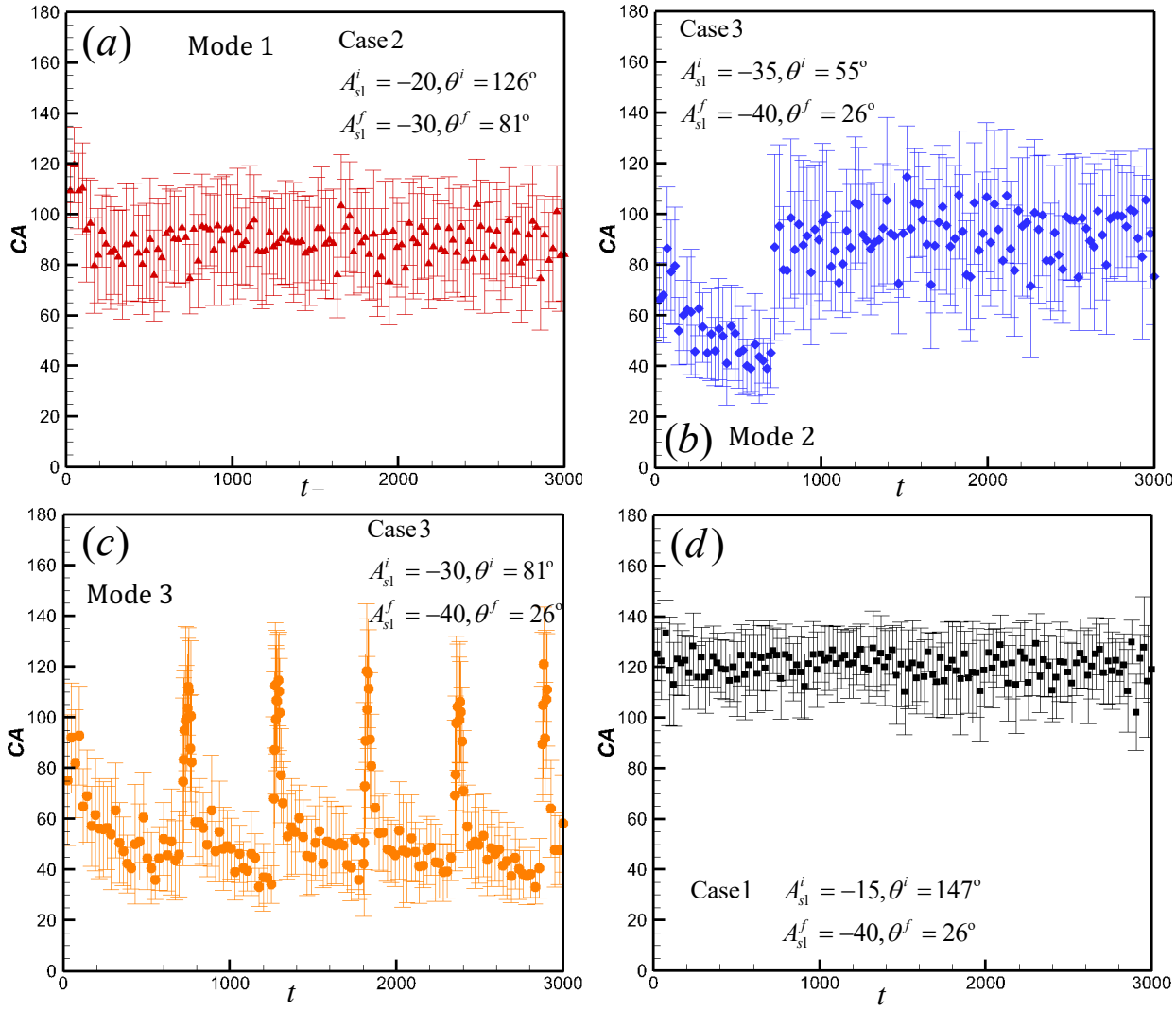

Fig. 4. Dynamic contact angles for different models of the electro-wetting bridge. (a-c) Modes 1 to 3, respectively. (d) Example unstable liquid bridge for certain original CAs.

The mode map of each case is provided in Fig. 5. The unstable LBs for Case 1 have been shown with dark diamond in Fig. 5a. It is worth mentioning that, although Mode 3 can be observed in Case 1 with $A_{s\ell}^i = -25$ ($\theta^i = 107°$) and $A_{s\ell}^f = -35$ or -40 ($\theta^f = 55°$ or $26°$), due to the fewer number of particles compared with Case 2 and 3, and lower energy compared with more hydrophobic initial conditions (e.g. $A_{s1}^i = -20$ ($\theta^f = 126°$) in Case 1), the two separated parts of the LB on each surfaces cannot meet each other as periodically as in other cases. Accordingly, these cases have not been included in the

analyses for height at break, H', and transfer ratio, R, shown later. The behaviors of Cases 2 and 3 are very similar to each other. Hence, one map is provided for both cases (Fig. 5b). In Fig. 5b, most of the continuous break and reformation cases (Mode 3) happen when the EW provides a final $A_{sl}^f = -40$ ($\theta^f = 26°$).

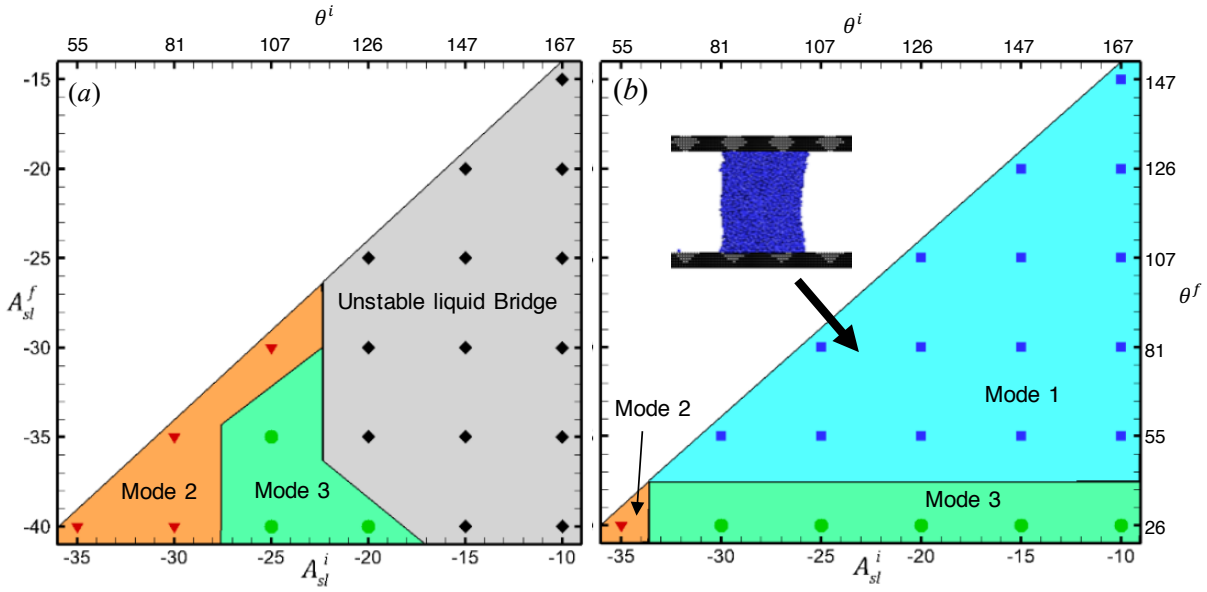

Fig. 5. Modes' maps for three different cases. (a) Case 1 and (b) Case 2 and 3. Blue square indicates Mode 1; Red delta indicates Mode 2; Green circle indicates Mode 3; Black diamond indicates unstable liquid bridge.

The period for bridge breaking and reformation in Mode 3 shows a strong correlation to bridge height. In order to generalize the present results, different LB heights or plate spacings (H_{LB} from 10 to 20 DPD length) are considered, but the ratio of the cube of bridge height to volume is kept constant at $H_{LB}^3/V = 0.253$. The initial and final contact angles in the test case in Fig. 3c and 4c are considered here. The droplet dynamics for these conditions are always in Mode 3. The intact bridge period τ_c, broken period τ_b, and the total duration of each cycle τ_t are reported. They monotonically increase with H^3 as shown in Fig. 6. This correlation suggests the ability to expand the results to other scales for similar operating conditions, e.g., operation contact angles.

The process of bridge breaking can also be characterized by the how the liquid is distributed following bridge breaking. We describe this distribution by the break height H' and transfer ratio R The break height, H', is defined as the distance from the bottom plate where the bridge initially breaks, and the transfer ratio R is defined as the ratio of liquid transferred to the lower surface after bridge breaking over the total initial volume of the LB. Figure 7 provides break height H' and transfer

ratio R versus A_{sl}^{i} (and the corresponding initial CA) for LBs showing Mode 3 dynamics. Because of the symmetric nature of the EWOD system for these cases, the break height is almost always at the middle of the two surfaces and the transfer ratio is around 0.5. However, due to the low volume of the liquid in Case 1, randomness has a substantial effect on the LB, and hence, the break height, and transfer ratio show some asymmetry.

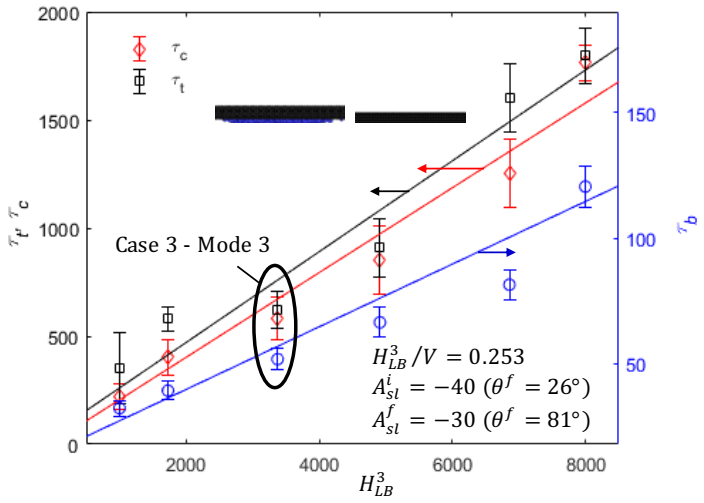

Fig. 6. Period of complete bridge, τ_c, bridge break, τ_b, and one cycle, τ_t, for Mode 3 using different liquid bridge height, H_{LB}. For all cases, $H_{LB}^{3}/N = 0.253$ and $A_{sl}^{i} = -30$ (θ^{i} =81°) & $A_{s\ell}^{f} = -40$ (θ^{f} =26°) as shown in mode's map.

To provide a visual illustration regarding the somewhat random behaviour of Case1, a case study with $A_{sl}^{i} = -25$ (θ^{i} =107°) and $A_{sl}^{f} = -40$ (θ^{f} = 26°) is considered in Fig. 8, which shows the center of mass versus time. As seen in this figure, the LB rupture and re-formation is not as periodic as previous examples provided in Fig. 3. This is likely due to the lower volumes of separated liquids on each surface and the lower potential energy provided in this case ($A_{sl}^{i} = -25$ (θ^{i} =107°)) compared with the case having $A_{sl}^{i} = -20$ (θ^{i} =126°) both of which increase the influence of the random fluctuations in force.

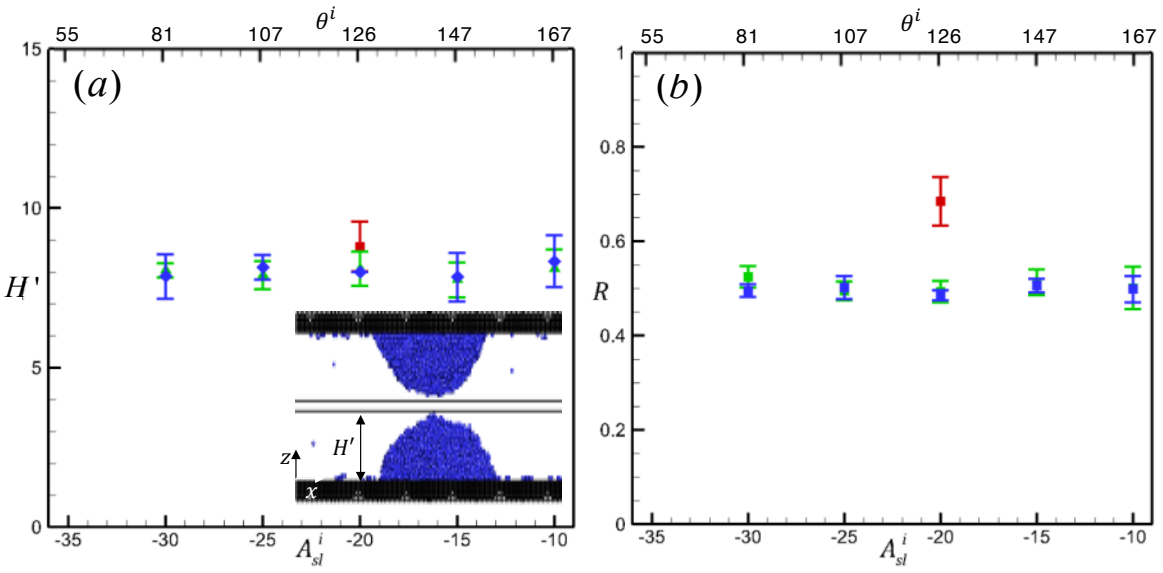

Fig. 7. Break height, H', (*a*) and mass ratio, R, (*b*), for Mode 3 using different cases and $A_{s1}^i(\theta^i)$. Red square, green triangle, and blue diamond are for Case 1 to 3, respectively. For all cases, $A_{s\ell}^f = -40\,(\theta^f = 26°)$ as shown in mode's map.

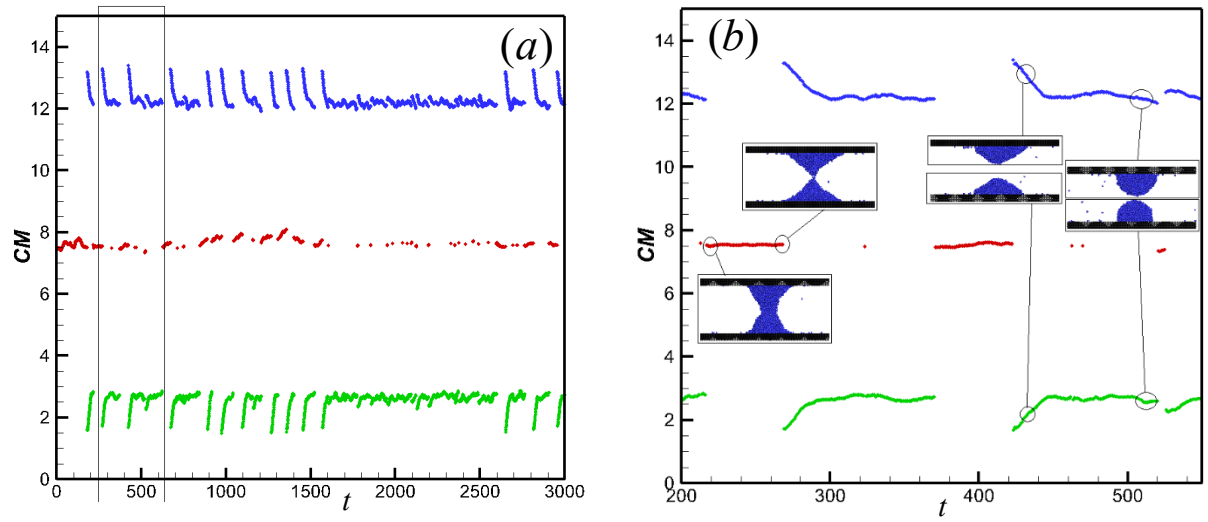

Fig. 8. Center of mass (CM) for Case 1 using $A_{s\ell}^i = -25\,(\theta^i = 107°)$ and $A_{s\ell}^f = -40\,(\theta^f = 26°)$. (*a*) shows the different behavior of liquid bridge at different times due to the effect of randomness originating from the smaller number of liquid beads compared with other cases. (*b*) shows a detailed illustration of the cycles.

4.*3. Asymmetric LB*

If the material properties of the upper and lower surfaces are different, the surface wettability and consequently the initial and final CAs of the liquid on upper and lower surfaces of the LB-EWOD

system are also different. Hence, an asymmetric LB is formed between the two surfaces and it breaks in an asymmetric fashion. This phenomenon has been schematically shown in Fig. 1b. The parameter space of the asymmetric LB is much larger due to the additional degree of freedom in surface wettability. Hence, the investigation of asymmetric LB-EWOD has been limited to five sub-cases provided in Table 4.

Table 4. Wettability parameters for upper and lower surfaces used for asymmetric investigations.

Case Number	**lower wall** $A_{s\ell}^{i} / \theta^{i}$	**upper wall** $A_{s\ell}^{i} / \theta^{i}$	**lower wall** $A_{s\ell}^{f} / \theta^{f}$	**upper wall** $A_{s\ell}^{f} / \theta^{f}$
Sub-case 1	-10/167°	-15/147°	-15/147°	-20/126°
Sub-case 2			-20/126°	-25/107°
Sub-case 3			-25/107°	-30/81°
Sub-case 4			-30/81°	-35/55°
Sub-case 5			-35/55°	-40/26°

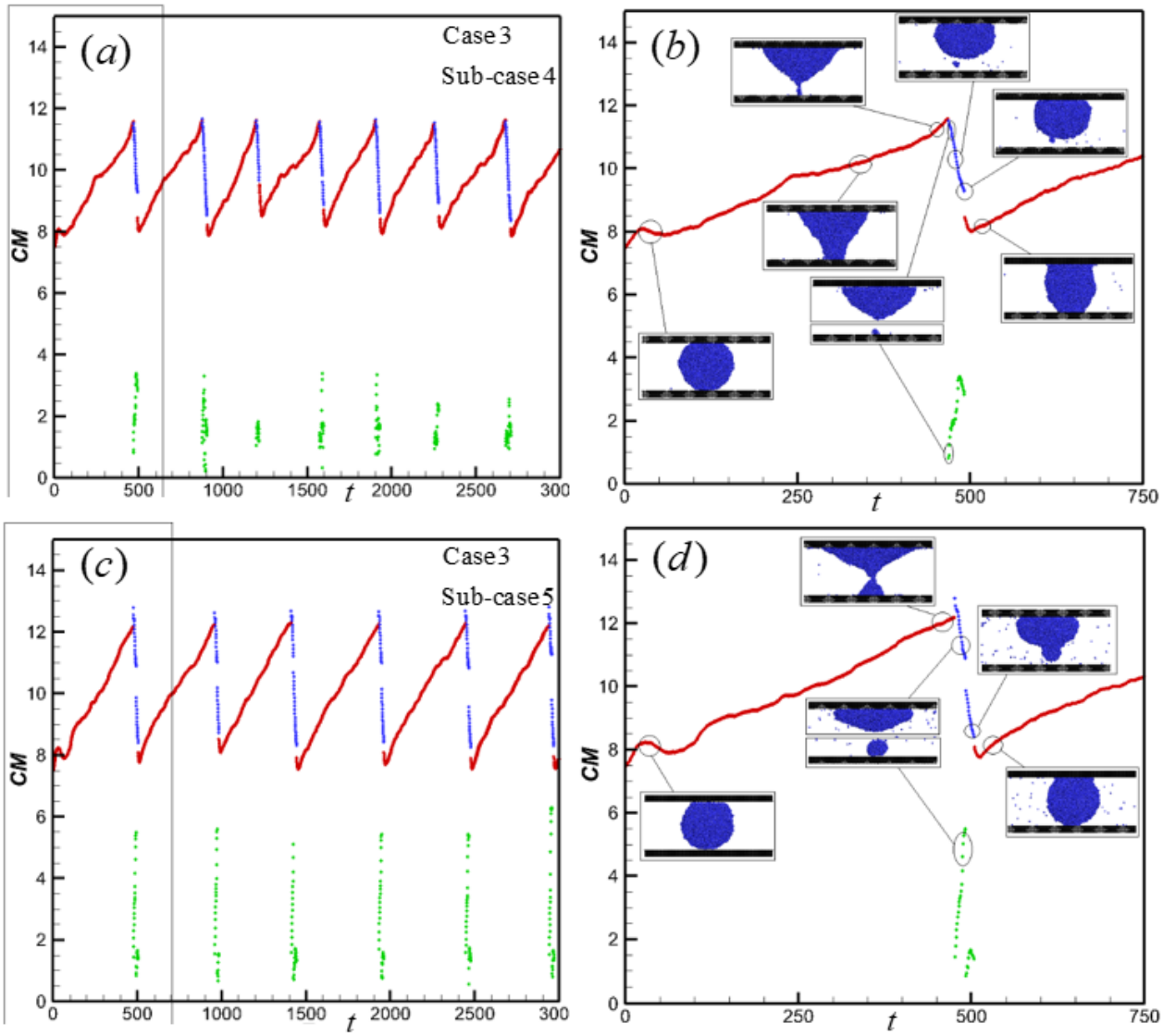

Fig. 9. Center of mass (CM) for two different asymmetric case studies (*a,c*), and an illustration of one cycle for each case (*b,d*).

Similar to symmetric cases, these asymmetric cases may break the bridge permanently, or may continuously break and re-form the LB. Samples of CM time histories are given in Fig. 9a and 9c for two case studies. The detailed illustration of one cycle for each case has been provided in Fig. 9b and 9d. In these two examples, a lower CA has been assigned to the upper wall and a higher CA has been assigned to the lower wall. It can be seen from the inset figures, in both cases, that, since the upper wall is more hydrophilic compared with the lower wall, the upper wall holds more liquid and the bridge breaks in a completely asymmetric configuration. As can be seen in both figures, the small amount of liquid on the lower wall may separate from the surface and form a satellite droplet. This

can be clearly seen in the inset in Fig. 9b. When the LB breaks, the electric field on the solid/liquid interface decreases and the initial CA is restored on each surface, and therefore the liquid recoils from the upper surface and again may form a bridge between the two surfaces. Supplementary Movie 02 shows the time history of a LB while it breaks and re-forms for the case given in Fig. 9a. If the volume of the liquid or the initial CA of the liquid on the surface is not favorable for bridge formation, the liquid may attach to the upper surface and may not form an LB. For geometric and material parameters used, this happens for all sub-cases of Case 1, which only has 5,508 beads. Similar to Fig. 3d, in these scenarios the initial LB is not stable, and hence this is not included within the available modes. The cases and their associated dynamic mode have been summarized in Table 4.

Table 5. Different modes of bridge behavior for studied asymmetric cases.

Sub-case Number / **Case number**	***Sub-case 1***	***Sub-case 2***	***Sub-case 3***	***Sub-case 4***	***Sub-case 5***
Case 1	---	---	---	---	---
Case 2	Mode 3	Mode 3	Mode 3	Mode 3	Mode 3
Case 3	Mode 1	Mode 1	Mode 3	Mode 3	Mode 3

In Fig. 10, the effect of LB height, H_{LB}, on the period of the oscillatory system dynamics is reported for the asymmetric system, with $H_{LB}^3/V = 0.253$ for Sub-case 4 for case 3. The figure shows the periods τ_c, τ_t and τ_c vs H_{LB}^3. Mode 3 was observed for all the simulations considered in this figure, and the periods are linearly increasing with H_{LB}^3. The periods are smaller and have larger variability compared with the symmetric data presented in Fig. 6. Also, since asymmetric case studies are more unstable, they may not follow a similar behavior of the symmetric ones, and hence decreasing trends is often seen for break and complete bridge periods in Fig. 10. The values of break height and transfer ratio for the asymmetric systems are given in Fig. 11. Because of the asymmetric nature, the break height H' is generally small and often approximately zero, $H' \approx 0$. Likewise $R \approx 0$ for almost all case studies as shown in Fig. 11b. In some cases in Fig. 11a, H' is not equal to zero, but the amount of liquid between the lower surface and the breakpoint is marginal and does not substantially affect the value of R. This phenomenon illustrated in the insets of Fig. 9b and 9d.

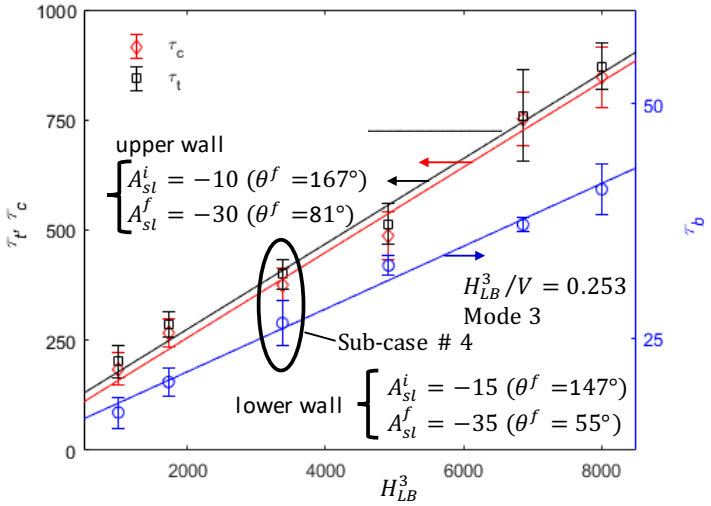

Fig.10. Period of complete bridge, τ_c, bridge break, τ_b, and one cycle, τ_t, for Sub-case 4 with different height, H_{LB}, and $H_{LB}^3/N = 0.253$.

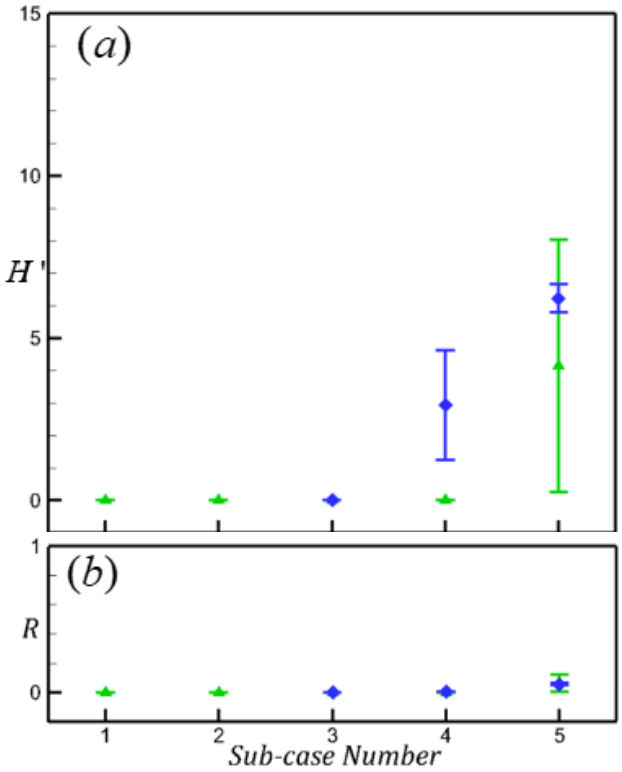

Fig.11. Break height (a) and mass ratio (b) for Mode 3 in Case 2 and 3 with wettability given in Table 5. Green triangles and blue diamonds are for Case 2 and 3, respectively.

5. Conclusion

A microscale liquid oscillator is proposed using EWOD. MDPD simulations have been conducted for both symmetric and asymmetric LBs with EWOD. By changing the wettability characteristics of the upper and lower surfaces, the LB's meniscus deforms. It was shown that depending on the modified wettability of the surfaces, the LB may or may not break. Three different dynamic modes for evolution of both symmetric and asymmetric LBs with respect to EWOD have been realized. Increasing the initial value of CA, i.e. increasing $A_{s\ell}^{i}$, increases the duration of time for which the bridge is complete and decreases the duration for which it is broken. The total time duration for one cycle is also changed for different values of $A_{s\ell}^{i}$. It was shown that LBs between plates with similar wettability usually rupture symmetrically, while for asymmetric LBs rupture mainly happens nearer the surface with lower wettability. Similar behaviour is seen in the ratio of liquid left on each surface after rupture. Satellite droplets have been observed in asymmetric cases. These droplets form from a small amount of liquid on the surface with low wettability, which jumps away from the surface when the wettability of the surface returns to its original value after the LB breaks. The data provided in this investigation can help to understand the fundamental physics behind the effects of EW between parallel surfaces. The results also provide design guidance for a microscale liquid oscillator using EWOD.

Acknowledgment

The support for our research by the National Science Foundation (Award Number: 1718194) is greatly appreciated.

References

[1] D. Yuan, Fundamentals and applications of inertial microfluidics: a review, Lab Chip. 16 (2016) 10–34. doi:10.1039/c5lc01159k.

[2] K. Choi, A.H.C. Ng, R. Fobel, A.R. Wheeler, Digital Microfluidics, Annu. Rev. Anal. Chem. 5 (2012) 413–440. doi:10.1146/annurev-anchem-062011-143028.

[3] E. Samiei, M. Tabrizian, M. Hoorfar, A review of digital microfluidics as portable platforms for lab-on a-chip applications, Lab Chip. 16 (2016) 2376–2396. doi:10.1039/c6lc00387g.

[4] Y. Li, C. Diddens, A. Prosperetti, K.L. Chong, X. Zhang, D. Lohse, Bouncing Oil Droplet in a Stratified Liquid and its Sudden Death, Phys. Rev. Lett. 122 (2019) 154502. doi:10.1103/PhysRevLett.122.154502.

[5] D. Quéré, Wetting and Roughness, Annu. Rev. Mater. Res. 38 (2008) 71–99. doi:10.1146/annurev.matsci.38.060407.132434.

[6] W.D. Kaplan, D. Chatain, P. Wynblatt, W.C. Carter, A review of wetting versus adsorption, complexions, and related phenomena: The rosetta stone of wetting, J. Mater. Sci. 48 (2013) 5681–5717. doi:10.1007/s10853-013-7462-y.

[7] P. Purswani, M.S. Tawfik, Z.T. Karpyn, Factors and Mechanisms Governing Wettability Alteration by Chemically Tuned Waterflooding: A Review, Energy and Fuels. 31 (2017) 7734–7745. doi:10.1021/acs.energyfuels.7b01067.

[8] M.E. Foulaadvand, N. Ojaghlou, Structural and elastic properties of a confined two-dimensional colloidal solid : A molecular dynamics study, 021405 (2012) 1–8. doi:10.1103/PhysRevE.86.021405.

[9] N. Ojaghlou, H. V. Tafreshi, D. Bratko, A. Luzar, Dynamical insights into the mechanism of a droplet detachment from a fiber, Soft Matter. 14 (2018). doi:10.1039/C8SM01257A.

[10] M. Abolghasemibizaki, C.J. Robertson, C.P. Fergusson, R.L. McMasters, R. Mohammadi, Rolling viscous drops on a non-wettable surface containing both micro- and macro-scale roughness, Phys. Fluids. 30 (2018). doi:10.1063/1.5016824.

[11] F. Mugele, J.C. Baret, Electrowetting: From basics to applications, J. Phys. Condens. Matter. 17 (2005). doi:10.1088/0953-8984/17/28/R01.

[12] L. Chen, E. Bonaccurso, Electrowetting - From statics to dynamics, Adv. Colloid Interface Sci. 210 (2014) 2–12. doi:10.1016/j.cis.2013.09.007.

[13] M. Abdelgawad, A.R. Wheeler, The Digital Revolution: A New Paradigm for Microfluidic, Adv. Mater. 21 (2009) 920–925. doi:10.1002/adma.200802244.

[14] M.W.J. Prins, W.J.J. Welters, J.W. Weekamp, Fluid control in multichannel structures by electrocapillary pressure, Science (80-.). 291 (2001) 277–280. doi:10.1126/science.291.5502.277.

[15] A.A. Hemeda, H.V. Tafreshi, General Formulations for Predicting Longevity of Submerged Superhydrophobic Surfaces Composed of Pores or Posts, (2014). doi:10.1021/la501894u.

[16] B. Berge, Électrocapillarité et mouillage de films isolants par l'eau, Comptes Rendus l'Académie Des Sci. Série II. 317 (1993) 157–163.

[17] D. Jiang, S.Y. Park, Light-driven 3D droplet manipulation on flexible optoelectrowetting devices fabricated by a simple spin-coating method, Lab Chip. 16 (2016) 1831–1839. doi:10.1039/c6lc00293e.

[18] G. McHale, C. V. Brown, M.I. Newton, G.G. Wells, N. Sampara, Dielectrowetting driven spreading of droplets, Phys. Rev. Lett. 107 (2011) 1–4. doi:10.1103/PhysRevLett.107.186101.

[19] F. Xia, Y. Zhu, L. Feng, L. Jiang, Smart responsive surfaces switching reversibly between super-hydrophobicity and super-hydrophilicity, Soft Matter. 5 (2009) 275–281. doi:10.1039/b803951h.

[20] S.J. Lee, J. Hong, K.H. Kang, I.S. Kang, S.J. Lee, Electrowetting-induced droplet detachment from hydrophobic surfaces, Langmuir. 30 (2014) 1805–1811. doi:10.1021/la404344y.

[21] K. Ashoke Raman, R.K. Jaiman, T.S. Lee, H.T. Low, A numerical study on electrowetting-induced jumping and transport of droplet, Int. J. Heat Mass Transf. 99 (2016) 805–821. doi:10.1016/j.ijheatmasstransfer.2016.04.038.

[22] A. Cavalli, D.J. Preston, E. Tio, D.W. Martin, N. Miljkovic, E.N. Wang, F. Blanchette, J.W.M. Bush, Electrically induced drop detachment and ejection, Phys. Fluids. 28 (2016). doi:10.1063/1.4940213.

[23] J. Hong, Y.K. Kim, K.H. Kang, J. Kim, S.J. Lee, Spreading dynamics and oil film entrapment of sessile drops submerged in oil driven by DC electrowetting, Sensors Actuators, B Chem. 196 (2014) 292–297. doi:10.1016/j.snb.2014.02.020.

[24] W.C. Nelson, P. Sen, C.J.C.J. Kim, Dynamic contact angles and hysteresis under electrowetting-on-dielectric, Langmuir. 27 (2011) 10319–10326. doi:10.1021/la2018083.

[25] E. Bormashenko, R. Pogreb, S. Balter, D. Aurbach, Electrically controlled membranes exploiting cassie-wenzel wetting transitions, Sci. Rep. 3 (2013) 1–5. doi:10.1038/srep03028.

[26] S. Wang, H.H. Chen, C.L. Chen, Electrowetting-on-dielectric assisted bubble detachment in a liquid film, Appl. Phys. Lett. 108 (2016). doi:10.1063/1.4948521.

[27] D. Baratian, A. Cavalli, D. Van Den Ende, F. Mugele, On the shape of a droplet in a wedge: New insight from electrowetting, Soft Matter. 11 (2015) 7717–7721. doi:10.1039/c5sm01511a.

[28] N. Li, L. Wu, C. Yu, H. Dai, T. Wang, Z. Dong, L. Jiang, Ballistic Jumping Drops on Superhydrophobic Surfaces via Electrostatic Manipulation, Adv. Mater. 30 (2018) 1–7. doi:10.1002/adma.201703838.

[29] S. Arscott, Electrowetting and semiconductors, RSC Adv. 4 (2014) 29223–29238. doi:10.1039/c4ra04187a.

[30] T. Krupenkin, J.A. Taylor, Reverse electrowetting as a new approach to high-power energy harvesting, Nat. Commun. 2 (2011) 447–448. doi:10.1038/ncomms1454.

[31] Y. Wang, H. Li, L. Zhao, B. Wu, S. Liu, Y. Liu, Optics & Laser Technology A review of droplet resonators : Operation method and application, Opt. Laser Technol. 86 (2016) 61–68. doi:10.1016/j.optlastec.2016.07.002.

[32] B. Berge, J. Peseux, Variable focal lens controlled by an external voltage: An application of electrowetting, Eur. Phys. J. E. 3 (2000) 159–163. doi:10.1007/s101890070029.

[33] S.K. Chung, K. Ryu, S.K. Cho, Electrowetting propulsion of water-floating objects, Appl. Phys. Lett. 95

(2009). doi:10.1063/1.3173197.

[34] S. Schuhladen, K. Banerjee, M. Stürmer, P. Müller, U. Wallrabe, H. Zappe, Variable optofluidic slit aperture, Light Sci. Appl. 5 (2016). doi:10.1038/lsa.2016.5.

[35] J. Hong, Y.K. Kim, D.J. Won, J. Kim, S.J. Lee, Three-dimensional digital microfluidic manipulation of droplets in oil medium, Sci. Rep. 5 (2015) 1–11. doi:10.1038/srep10685.

[36] T.H. Hsu, S. Manakasettharn, J.A. Taylor, T. Krupenkin, Bubbler: A Novel Ultra-High Power Density Energy Harvesting Method Based on Reverse Electrowetting, Sci. Rep. 5 (2015) 1–13. doi:10.1038/srep16537.

[37] B. Roman, J. Bico, Elasto-capillarity: Deforming an elastic structure with a liquid droplet, J. Phys. Condens. Matter. 22 (2010). doi:10.1088/0953-8984/22/49/493101.

[38] A. Klingner, S. Herminghaus, F. Mugele, Self-excited oscillatory dynamics of capillary bridges in electric fields, Appl. Phys. Lett. 82 (2003) 4187–4189. doi:10.1063/1.1580995.

[39] P. Español, P.B. Warren, Perspective: Dissipative particle dynamics, J. Chem. Phys. 146 (2017). doi:10.1063/1.4979514.

[40] A. Ghoufi, J. Emile, P. Malfreyt, Recent advances in Many Body Dissipative Particles Dynamics simulations of liquid-vapor interfaces., Eur. Phys. J. E. Soft Matter. 36 (2013) 10. doi:10.1140/epje/i2013-13010-7.

[41] A. Boromand, S. Jamali, J.M. Maia, Viscosity measurement techniques in Dissipative Particle Dynamics, Comput. Phys. Commun. 196 (2015) 149–160. doi:10.1016/j.cpc.2015.05.027.

[42] A. Ghoufi, P. Malfreyt, Mesoscale modeling of the water liquid-vapor interface: A surface tension calculation, Phys. Rev. E - Stat. Nonlinear, Soft Matter Phys. 83 (2011) 1–5. doi:10.1103/PhysRevE.83.051601.

[43] E. Abu-Nada, Dissipative particle dynamics simulation of combined convection in a vertical lid driven cavity with a corner heater, Int. J. Therm. Sci. 92 (2015) 72–84. doi:10.1016/j.ijthermalsci.2015.01.022.

[44] L. Lei, E. Louis, B. Cheong, N. Phan-thien, Many-body dissipative particle dynamics (MDPD) simulation of a pseudoplastic yield-stress fluid with surface tension in some flow processes, J. Nonnewton. Fluid Mech. 260 (2018) 163–174. doi:10.1016/j.jnnfm.2018.07.006.

[45] A. Mishra, A.A. Hemeda, M. Torabi, J. Palko, S. Goyal, D. Li, Y. Ma, A simple analytical model of complex wall in multibody dissipative particle dynamics, J. Comput. Phys. (2019). doi:https://doi.org/10.1016/j.jcp.2019.06.075.

[46] P.B. Warren, Vapor-liquid coexistence in many-body dissipative particle dynamics, (2003) 1–8. doi:10.1103/PhysRevE.68.066702.

[47] M. Ahmadlouydarab, C. Lan, A.K. Das, Y. Ma, Coalescence of sessile microdroplets subject to a wettability gradient on a solid surface, Phys. Rev. E. 94 (2016) 1–12. doi:10.1103/PhysRevE.94.033112.

[48] K.C. Ng, T.W.H. Sheu, Refined energy-conserving dissipative particle dynamics model with

temperature-dependent properties and its application in solidification problem, Phys. Rev. E. 96 (2017) 1–12. doi:10.1103/PhysRevE.96.043302.

[49] M. Arienti, W. Pan, X. Li, G. Karniadakis, Many-body dissipative particle dynamics simulation of liquid/vapor and liquid/solid interactions, J. Chem. Phys. 134 (2011). doi:10.1063/1.3590376.

[50] Z. Li, X. Bian, Y. Tang, G. Em, A dissipative particle dynamics method for arbitrarily complex geometries, J. Comput. Phys. 355 (2018) 534–547. doi:10.1016/j.jcp.2017.11.014.

[51] M.P. Allen, D.J. Tildesley, Computer Simulation of Liquids, Second, Oxford University Press, 2017.

[52] K. Zhang, Z. Li, M. Maxey, S. Chen, G.E. Karniadakis, Self-Cleaning of Hydrophobic Rough Surfaces by Coalescence- Induced Wetting Transition, 35 (2019). doi:10.1021/acs.langmuir.8b03664.

[53] B.-Y. Cao, M. Chen, Z.-Y. Guo, Liquid flow in surface-nanostructured channels studied by molecular dynamics simulation, Phys. Rev. E. 74 (2006) 066311. doi:10.1103/PhysRevE.74.066311.

[54] G.S. Jung, J.S. Lee, Y.H. Won, Effects of liquid property and substrate roughness on the response time of an electrowetting liquid lens, 1054516 (2018) 40. doi:10.1117/12.2286273.

[55] M. Torabinia, A. Farzbod, H. Moon, Electromechanical model to predict the movability of liquids in an electrowetting-on-dielectric microfluidic device, J. Appl. Phys. 123 (2018). doi:10.1063/1.5014045.

[56] C.C. Chang, Y.J. Sheng, H.K. Tsao, Wetting hysteresis of nanodrops on nanorough surfaces, Phys. Rev. E. 94 (2016) 1–8. doi:10.1103/PhysRevE.94.042807.

[57] A.A. Hemeda, R.J.A. Esteves, J.T. McLeskey, M. Gad-el-Hak, M. Khraisheh, H. Vahedi Tafreshi, Molecular Dynamic Simulations of Fibrous Distillation Membranes, Int. Commun. Heat Mass Transf. 98 (2018) 304–309. doi:10.1016/j.icheatmasstransfer.2018.09.012.

[58] P.B. Paramonov, S.F. Lyuksyutov, Density-functional description of water condensation in proximity of nanoscale asperity, J. Chem. Phys. 123 (2005). doi:10.1063/1.2007632.